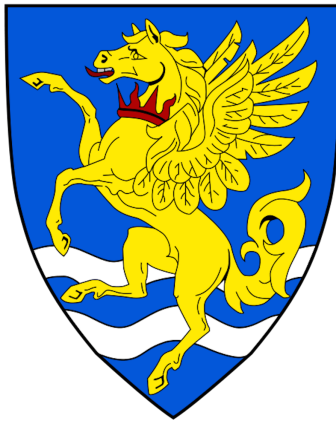


APPROACHING THE MARANGONI EFFECT
THROUGH
EQUILIBRIUM MOLECULAR DYNAMICS

HUGH GRAHAM ALEXANDER BURTON
ROBINSON COLLEGE
CAMBRIDGE



Declaration

This dissertation is submitted in partial fulfilment of the requirements for Part III Chemistry. It describes work carried out in the Department of Chemistry in the Michaelmas Term 2015 and the Lent Term 2016. Unless otherwise indicated, the research described is my own and not the product of collaboration.

Acknowledgements

This project could not have been completed without the encouragement of a number of people ranging from department colleagues to friends and family. In particular, I would like to thank Raman Ganti who provided endless support and excellent supervision throughout. Finally, I pass on many thanks to Daan Frenkel for the opportunity to work with his group, and for his advice and comments which have inspired so much of this work.

APPROACHING THE MARANGONI EFFECT THROUGH EQUILIBRIUM MOLECULAR DYNAMICS

H. G. A. BURTON

Abstract

The Marangoni flow induced by a temperature gradient at a liquid–liquid interface was studied through the use of equilibrium molecular–dynamics simulations for a symmetric Lennard–Jones binary–mixture. An artificial Marangoni force was computed by considering the finite difference in the transverse component of the stress–tensor for two equilibrium simulations at different temperatures. Applying this as a body force to a third equilibrium simulation at an intermediate temperature allowed the Marangoni flow profile to be computed.

This was demonstrated for a binary–mixture confined within a piston and a binary–mixture periodic in all dimensions. Because the atomic stress–tensor is not uniquely defined, the use of the Virial and Irving–Kirkwood stress–tensor was compared. Finally, this method was used to study the effect of added surfactant molecules at the interface, and a retardation of the Marangoni flow was observed.

Contents

Declaration	i
Acknowledgements	i
Abstract	ii
1 Introduction	1
1.1 Experimental studies	2
1.2 Striving for a microscopic description	2
2 Theoretical Background	4
2.1 The macroscopic description	4
2.2 A microscopic approach	5
2.3 The Finite Difference Approach	6
2.4 Non-uniqueness of the pressure tensor	6
3 Experimental Details	8
3.1 Interaction Model	8
3.2 Reduced Units	9
3.3 Thermostats	9
3.4 Barostats	10
3.5 Preparing the system	10
3.6 Calculating the stress tensor	11
3.7 Computing averages	11
3.8 Modelling surfactant molecules	12
3.9 Software details	13
4 Results and Discussion	14
4.1 Binary-mixture confined between two walls	14
4.1.1 Comparing to the Irving-Kirkwood stress	17
4.2 Binary-mixture periodic in 3-dimensions	20
4.2.1 Comparing the virial and Irving-Kirkwood stress	21
4.2.2 Reducing the noise in the force-profile	24
4.3 The effect of surfactants	27

5	Concluding Remarks	32
5.1	Future directions of study	33
	Bibliography	35

1 Introduction

Interfacial flows resulting from a chemical potential or temperature gradient were first reported by J. Thompson in 1855.¹ After forming the basis of Carlo Marangoni’s doctoral dissertation in 1865, this phenomenon was termed the “Marangoni Effect”.² Subsequently, many scientific studies have focused on temperature induced Marangoni flows, also known as thermocapillary motion

Through the works of Derjaguin et al.³ and Levich⁴, a thorough macroscopic description has been developed. Anderson summarises these results in the context of phoresis.⁵

The Marangoni effect can be described as resulting from an interfacial tension gradient. Experimental studies indicate hot fluids have a lower surface tension than cold fluids,^{6,7} inducing motion in the opposite direction to a temperature gradient. However, this analysis does not progress far since the temperature dependence of surface tension is not rigorously understood.

Levich used hydrodynamics to derive the fluid velocity across a shallow pan in terms of $\partial\gamma/\partial T$.⁴ He achieved this using a continuity equation setting the total flow to zero. This implied that any interfacial flows are accompanied by an opposing flow in the bulk fluid.

In contrast, Derjaguin et al. calculated the momentum flux from a temperature gradient by computing the energy flux carried by pressure-driven convection and applying Onsager’s reciprocal rule.³ They showed that the velocity can be related to the excess enthalpy density near the interface (relative to the bulk), yielding a macroscopic description.

However, these theories are founded upon a thermodynamic backbone which relies on knowledge of the macroscopic system. Marangoni flows are a microscopic phenomenon, localised at fluid interfaces, and cannot be faithfully described using thermodynamics. Instead, a microscopic theory using interparticle interactions is required. No such theory currently exists, and there has been limited research in this area.⁸

By studying the microscopic properties of a liquid–liquid interface, this report aims to model the Maragnoni effect and investigate the link between microscopic fluid properties and its macroscopic motion.

1.1 Experimental studies

Despite the lack of a microscopic theory, there has been substantial experimental research into the Marangoni effect. Many studies have focussed on the more curious examples of Marangoni flows, including Thompson’s “tears of wine”^{1,9–11} and the “coffee ring effect”,^{12–14} whilst others demonstrate its importance in technology. For example, Sternling and Scriven¹⁵ proposed Marangoni effects as the origin of interfacial turbulence and mass transport, yielding applications in fluid mixing and oil recovery.^{16–18} Furthermore, Subramanian and Balasubramanian outlined the importance of Marangoni forces for the motion of bubbles and droplets in reduced gravity.¹⁹

In 1959, Young et al. produced a theoretical description of this motion of bubbles and droplets due to a temperature gradient, a phenomenon termed thermophoresis.²⁰ They described how this gradient causes a higher surface tension on the low temperature side of the droplet, creating a force pulling the surrounding fluid towards this region. A corresponding reaction force then propels the droplet towards the warmer fluid. Analogously to electrophoresis, no net force acts on the fluid within the droplet.

This was measured experimentally by S. C. Hardy,²¹ who used a temperature gradient to balance the Marangoni and buoyancy forces acting on a droplet within a fluid, thus holding the droplet stationary. Later theoretical modelling by Kim and Subramanian suggested that the inclusion of surfactants could prevent thermophoresis,^{22,23} a prediction subsequently confirmed experimentally.^{24,25}

With the advances in space technology, thermophoresis and thermocapillary motion have become important mechanisms for fluid motion and mass transfer in low-gravity environments, where surface effects dominate over buoyancy driven motion. The motion of bubbles and drops due to interfacial gradients is considered key for materials processing in space, enabling phase separation of mixtures and the potential to make uniform composite materials.²⁴ Moreover, fluid transport in the absence of gravity is important for controlling fluids aboard satellites.

1.2 Striving for a microscopic description

With many potential applications, the search for a microscopic description is becoming ever more significant, and computer simulations are increasingly being used to understand this phenomenon. Marangoni flows are dynamic and can be stud-

ied using a time-dependent method such as molecular dynamics. Modelling the behaviour of a partially miscible binary-mixture under the effect of a temperature gradient might appear trivial; create a temperature gradient in a system and measure the subsequent particle velocities. Hampe et al. used this non-equilibrium approach in their study of the Marangoni effect.⁸ Despite positive results, this method is complicated by periodic boundary conditions that require the simulation box to have two temperature gradients, creating a periodic temperature gradient. Any induced flow then generates an opposing concentration gradient, and an equilibrium state is reached.

In the present study, we investigate the use of equilibrium molecular dynamics simulations for modelling the Marangoni effect. By calculating the equilibrium stress acting on a binary-mixture for two different temperatures, the temperature derivative of the transverse stress can be estimated and used to compute a body force. This can then be applied in a simulation at an intermediate temperature to imitate the Marangoni force, thus circumventing the complications of a periodic temperature profile. By measuring the velocity profile in this final simulation, Marangoni flows can be observed.

Using this equilibrium method, we show that a Marangoni force at a liquid-liquid interface can be calculated from the transverse stress tensor and used to generate a Marangoni flow. The effect of surfactants on the magnitude of this flow is then investigated.

A theoretical description of the Marangoni effect is described in Section 2, whilst Section 3 outlines the computational methods used. The simulation results are discussed in Section 4. Section 5 summarises the conclusions and proposes directions for future studies.

2 Theoretical Background

2.1 The macroscopic description

The motion of fluids may be described macroscopically using the Navier–Stokes equation.²⁶ This models liquids as a continuous medium and combines the conservation of mass and momentum with the relation between the force on a volume element and the local fluid flow. In the low Reynolds-number regime the flow velocity is small, and the Navier–Stokes equation reduces to

$$\eta \nabla^2 \mathbf{v}(r, t) = \nabla P(r, t) - \mathbf{f}(r). \quad (1)$$

Equation 1 shows that motion in fluids *can only* occur through a pressure gradient or external forces. In Marangoni flows, motion from a temperature gradient must result from induced local pressure gradients, which may be derived from thermodynamics.

Consider a binary–mixture with an interface at $z = 0$. The Gibbs–Duhem equation gives

$$V dP = \sum_{i=0}^n N_i d\mu_i + S dT. \quad (2)$$

The bulk fluid pressure is constant and isotropic, giving

$$\left(\frac{\partial P}{\partial x} \right) = \sum_{i=0}^n \rho_i^B \left(\frac{\partial \mu_i}{\partial x} \right) + \frac{S}{V} \left(\frac{\partial T}{\partial x} \right) = 0. \quad (3)$$

The Maxwell relations relate the entropy to the partial differential of chemical potential with respect to temperature through

$$\left(\frac{\partial \mu_i}{\partial T} \right)_{P, N_i} = - \left(\frac{\partial S}{\partial N_i} \right)_{P, T}. \quad (4)$$

The total entropy is the weighted sum of the partial entropy of each species in the system,

$$S = \sum_{i=0}^n s_i N_i, \quad (5)$$

thus

$$\left(\frac{\partial \mu_i}{\partial T} \right)_{P, N_i} = -s_i. \quad (6)$$

This allows Equation 3 to be expressed as

$$\left(- \sum_{i=1}^n \rho_i^B s_i + \frac{S^B}{V} \right) \left(\frac{\partial T}{\partial x} \right) = 0, \quad (7)$$

for which the solution is

$$\frac{S^B}{V} = \sum_{i=1}^n \rho_i^B s_i^B. \quad (8)$$

Consider the case close to an interface where the pressure will deviate from its bulk value. Since μ_i and T are independent of z ,

$$\left(\frac{\partial \mu_i}{\partial T} \right) = -s_i^B, \quad (9)$$

and the pressure gradient reduces to

$$\left(\frac{\partial P(z, x)}{\partial x} \right) = \left(\sum_{i=1}^n \rho_i(z) (s_i(z) - s_i^B) \right) \left(\frac{\partial T}{\partial x} \right). \quad (10)$$

For an ideal mixture, the partial entropy is given by $s_i = \frac{1}{T} (\mu_i - h_i)$, and Equation 10 can be expressed in terms of the excess enthalpy density, $\Delta h(z)$,

$$\left(\frac{\partial P(z, x)}{\partial x} \right) = -\Delta h(z) \frac{1}{T} \left(\frac{\partial T}{\partial x} \right) = -\Delta h(z) \left(\frac{\partial \ln T}{\partial x} \right). \quad (11)$$

Substituting Equation 11 into Equation 1 and assuming a constant pressure in the (z, y) directions allows the velocity, $v_x(z)$, at the interface to be computed as

$$v_x(z=0) = -\frac{1}{\eta} \int_0^\infty dz z \Delta h(z) \frac{\partial T}{\partial x} \quad (12)$$

where it has been assumed that the bulk fluid is at rest ($v_x(z=\infty) = 0$). This expression is almost equivalent to that derived by Derjaguin et al., except for a factor of two, suggesting a potential error in Derjaguin's approach.^{3,5}

2.2 A microscopic approach

The Marangoni effect occurs on microscopic length-scales, and hence a macroscopic approach is not entirely appropriate. Instead of solving the Navier-Stokes equation, the velocity should be related directly to the local forces acting on the fluid, which may be calculated from the local stress tensor,

$$f_x(z) = - \left(\frac{\partial \sigma_{xx}(z, x)}{\partial x} \right). \quad (13)$$

The Marangoni force occurs due to temperature gradients and $f_x(z)$ can be calculated through the chain rule as

$$f_x(z) = - \left(\frac{\partial \sigma_{xx}(z, x)}{\partial T} \right) \left(\frac{\partial T}{\partial x} \right). \quad (14)$$

2.3 The Finite Difference Approach

Equation 14 demonstrates that the Marangoni force can be inferred from the temperature dependence of the stress tensor. To a first order approximation, the temperature gradient of the stress tensor can be estimated from a finite difference as

$$\left(\frac{\partial \sigma_{xx}(z, x)}{\partial T}\right) \approx \frac{\sigma_{xx}^{T_2}(z, x) - \sigma_{xx}^{T_1}(z, x)}{T_2 - T_1}. \quad (15)$$

Using this approximation, the Marangoni flow profile can be computed as follows:

1. Compute $\sigma_{xx}(z)$ for an equilibrium system at temperature T_1 .
2. Repeat the calculation for another equilibrium system at a slightly higher temperature T_2 .
3. Approximate the partial derivative of the transverse stress with respect to temperature using the finite difference, Equation 15.
4. Infer $f_x(z)$ for a specified value of $\partial T / \partial x$ using Equation 14.
5. Compute the flow profile by applying $f_x(z)$ as a body force in an equilibrium simulation at an intermediate temperature T_3 (where $T_1 < T_3 < T_2$).

2.4 Non-uniqueness of the pressure tensor

The stress tensor is related to the pressure tensor through

$$\sigma_{\alpha\beta}(\mathbf{r}) = -P_{\alpha\beta}(\mathbf{r}). \quad (16)$$

The pressure tensor is composed of a kinetic contribution, arising from the momentum transfer of particles on the container walls, and a potential contribution attributed to the interparticle forces.²⁷ The kinetic part is calculated from the ideal gas contribution,

$$\mathbf{P}^K(\mathbf{r}) = k_B T \rho(\mathbf{r}) \hat{\mathbf{I}}, \quad (17)$$

whilst the potential contribution cannot be uniquely defined.

For a homogeneous fluid the stress tensor is isotropic, with each diagonal element equal to $-P$, where P is the bulk hydrostatic pressure. This pressure can be calculated using the virial equation, originally derived from Clausius' virial theorem²⁸

(also derivable by differentiating the canonical partition function²⁹), to give

$$P_{\alpha\beta}(\mathbf{r}) = \frac{1}{V} \left(-m(\mathbf{r}) \langle \nu_\alpha \nu_\beta \rangle + \frac{1}{2} \sum_i^N \sum_{j \neq i}^N (r_\alpha^{(i)} - r_\alpha^{(j)}) f_\beta^{ij} \right). \quad (18)$$

Clausius' formulation calculates the local pressure by considering the forces acting on particles located within a volume element at \mathbf{r} .

In an inhomogeneous system there is an ambiguity over which particles should contribute to the force at a given position.^{27,29,30} This was first discussed by Irving and Kirkwood^{31,32} who described an alternative method that computes the pressure tensor from the forces acting across an infinitesimal surface $d\mathbf{A}$ located at \mathbf{r} . They calculate the local pressure tensor using only pairs of particles for which the line connecting their centers of mass passes through $d\mathbf{A}$. For a planar system with an interface in the (x, y) plane, the pressure tensor depends only on the distance from this interface and the normal and tangential components are given by

$$P_N^{\text{IK}}(z) = \rho(z) k_B T - \frac{1}{2A} \left\langle \sum_{i \neq j} \frac{|z_{ij}|}{r_{ij}} U'(r_{ij}) \Theta \left(\frac{z - z_i}{z_{ij}} \right) \Theta \left(\frac{z_j - z}{z_{ij}} \right) \right\rangle, \quad (19)$$

$$P_T^{\text{IK}}(z) = \rho(z) k_B T - \frac{1}{4A} \left\langle \sum_{i \neq j} \frac{x_{ij}^2 + y_{ij}^2}{r_{ij}} \frac{U'(r_{ij})}{|z_{ij}|} \Theta \left(\frac{z - z_i}{z_{ij}} \right) \Theta \left(\frac{z_j - z}{z_{ij}} \right) \right\rangle. \quad (20)$$

For studying confined systems, the Irving–Kirkwood stress has many advantages. In particular it yields a normal component independent of local fluctuations in the number density. Density fluctuations occur close to walls due to structural layering of the fluid, and there is reduced density at liquid–liquid interfaces from the finite width of the interfacial region. Consequently, the normal component of the virial pressure oscillates²⁷ whilst the Irving–Kirkwood normal component is constant and equal to the bulk hydrostatic pressure. This is more consistent with intuition since the fluid is isotropic in the direction normal to surfaces.

3 Experimental Details

Equilibrium molecular dynamics simulations of a symmetric binary-mixture of partially miscible fluids were used to measure the stresses acting on the fluid at two different temperatures. The Marangoni force was then inferred using Equation 15. Where possible, this force was applied as a body force in a simulation at an intermediate temperature to generate a Marangoni flow profile.

Two key systems were studied, a symmetric binary-mixture under three-dimensional periodic boundary conditions, and a binary-mixture periodic in the (x, y) plane but confined between two walls in the z -dimension, as shown in Figure 1. All molecular dynamics simulations were executed using the LAMMPS (Large Atomic and Molecular Massively Parallel Simulator) package.³³

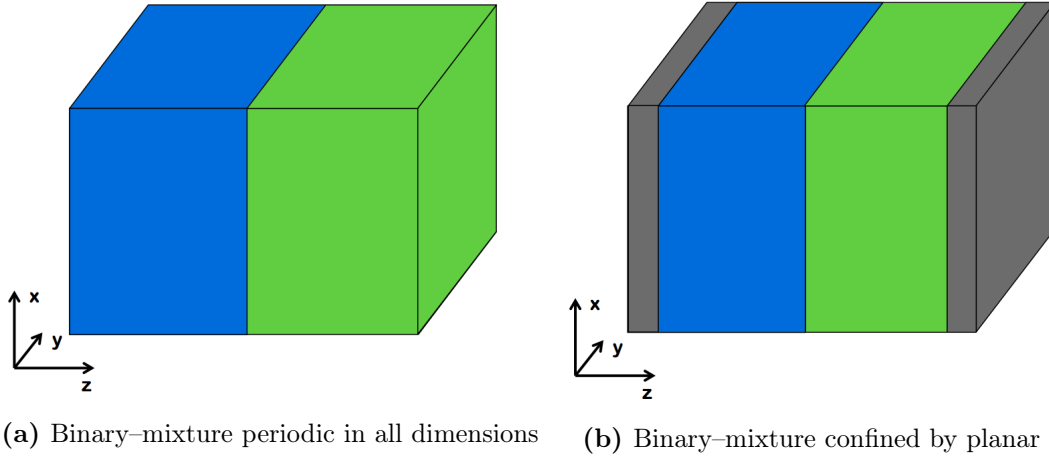


Figure 1: Both the systems studied incorporated a partially miscible binary-mixture of Fluid A (blue) and Fluid B (green). For the mixture periodic in all dimensions, the pressure is regulated using a Nosé-Hoover barostat. In the confined fluid, the walls are used to create a piston and an external force equal to $P_{\text{ext}} \times A_{\text{wall}}$ is applied.

3.1 Interaction Model

The fluids were modelled using spherical particles and their interaction was tuned to a pair-wise truncated Lennard-Jones potential:

$$V(\mathbf{r}^N) = \frac{1}{2} \sum_{i \neq j} \phi(r_{ij}) \quad (21)$$

where

$$\phi(r_{ij}) = 4\epsilon_{ij} \left(\left(\frac{\sigma_{ij}}{r_{ij}} \right)^{12} - \left(\frac{\sigma_{ij}}{r_{ij}} \right)^6 \right) \text{ for } r \leq r_c \quad (22)$$

$$\phi(r_{ij}) = 0 \text{ for } r > r_c. \quad (23)$$

This potential includes an attractive r_{ij}^{-6} term accounting for long-range dispersion forces and a short-range r_{ij}^{-12} repulsive term corresponding to the Pauli repulsion between particles. The length-scale of the potential is given by σ_{ij} (set as equal for all i and j) while ϵ_{ij} determines the strength of the interaction.

The miscibility of the two fluids (A and B) was controlled using the relative values of the interaction parameter. The values chosen were:

$$\epsilon_{A,A} = \epsilon_{B,B} = 1.0, \quad (24)$$

$$\epsilon_{A,B} = 0.55, \quad (25)$$

in agreement with previous studies on Lennard-Jones binary-mixtures.^{8,34,35} The cutoff for the potential was $r_c = 4 \sigma$.

3.2 Reduced Units

Physical quantities including distances and energies are expressed in terms of reduced units. For a Lennard-Jones system, the basic units are σ for length, ϵ for energy and m for mass, from which all other units may be derived.³⁶ Physical quantities become dimensionless when expressed in terms of these units, for example $r^* \equiv r/\sigma$. Scaled coordinates expressed relative to the simulation box size are also used, for example $z' = z^*/L_z^*$ where L_z^* is the dimension of the box in the z -direction. These are useful if the box-dimensions vary, such as when a barostat acts on the system.

3.3 Thermostats

In molecular dynamics simulations, the temperature is controlled using thermostats, which simulate the coupling of the system to an external heat bath.

Thermostats work by applying a stochastic frictional force to particles, either by adding a random force to momenta (Langevin)³⁷ or reassigning the velocity of randomly chosen particles to that obtained from the Maxwell distribution (Andersen)³⁸.

The Nosé–Hoover thermostat was used throughout this study. This introduces a fictitious frictional force into the equations of motion, adjusting the particle velocities until the temperature is equal to the desired value.^{39–41} The equations of motion in three–dimensions become:

$$m_i \frac{d^2 \mathbf{r}}{dt^2} = \mathbf{f}_i - \zeta m_i \mathbf{v}_i \quad (26)$$

$$\frac{d\zeta(t)}{dt} = \frac{1}{Q} \left[\sum_{i=1}^N m_i \frac{\mathbf{v}_i^2}{2} - \frac{3N+1}{2} k_B T \right]. \quad (27)$$

The result is a system where the energy fluctuates but the combined energy of the system and heat bath remains constant, maintaining a canonical ensemble.

3.4 Barostats

The bulk pressure of the fluid must also be held constant. A piston provides the simplest method; the fluid is confined between two solid walls and a force equal to $P_{ext} \times A_{wall}$ is applied. This was used for studying the binary–mixture confined between two walls. Under a temperature gradient, a thermocapillary effect also occurs at the liquid–solid surface. The interface must be sufficiently far from the walls such that this can be ignored.

Alternatively a Nosé–Hoover barostat regulates the pressure by adjusting the simulation box dimensions and altering the equations of motion accordingly.^{39–41} When studying surface effects, the box size must only be changed in the direction perpendicular to the interface. A change parallel to the interface its area and create an error in the thermodynamic pressure,

$$P = - \left(\frac{\partial F}{\partial V} \right)_T + \gamma \left(\frac{\partial A}{\partial V} \right)_T. \quad (28)$$

3.5 Preparing the system

The fluid was prepared from a face–centred cubic lattice with a spacing of 1.64414σ and a simulation box size of $L_x^* = 13.1531$, $L_y^* = 13.1531$ and $L_z^* = 32.8828$. This lattice was melted over 2×10^6 timesteps of length 0.001τ to generate a fluid state. The pressure was $P^* = 0.1$ and the temperatures used were $T^* = 0.8$ and $T^* = 0.9$, ensuring the system occupied the liquid region of the Lennard–Jones phase space.⁴² Solid walls were constructed with a harmonically bonded lattice using a spring constant of $K^* = 2500$ and an equilibrium bond length of $r_0^* = 1.163$.

3.6 Calculating the stress tensor

The virial stress tensor was calculated using an in-built function within the LAMMPS package, which returns the stress tensor for each atom. However, LAMMPS does not have a method for calculating the Irving–Kirkwood stress tensor. Instead this was calculated by saving the particle positions on a given timestep to a file. The stress tensor was then computed using a programme written by R. Ganti and adapted for the specific systems studied. Since the virial method is implemented in parallel whilst the Irving–Kirkwood method is not, computing the Irving–Kirkwood stress incurred approximately a 4-fold increase in computational time.

3.7 Computing averages

Usually time-averages of physical observables are calculated in molecular dynamics simulations. In this study, the observables are the number density, stress tensor and particle velocities. Their values were measured on every timestep and spatially averaged into 400 planar slabs across the z -dimension of the box. These spatial averages were then time-averaged over the full simulation.

Under the ergodic hypothesis, time-averages can be equated to ensemble averages for an infinitely long simulation time.⁴³ Practically, however, these averages are evaluated over a finite time period, and have a statistical error. The method of block-averaging, developed by Flyvbjerg and Peterson, provides an efficient technique for computing this error.⁴⁴ They show that the variance of an observable, A , can be estimated by

$$\text{var}(A) \geq \left\langle \frac{C_0}{n-1} \right\rangle, \quad (29)$$

where C_0 is the value of the time-correlation function for the block-transformed data at $t = 0$ given by

$$C_0 \equiv \frac{1}{n} \sum_{k=1}^n (A_k - \bar{A}) (A_k - \bar{A}). \quad (30)$$

A lower bound for the variance can be calculated by finding the block length where this estimate plateaus. Furthermore, the error in the variance can be estimated as

$$\sqrt{\frac{2}{n-1} \times \frac{C_0}{n-1}}. \quad (31)$$

A blocking-analysis for a binary-mixture identical to those used throughout this study was executed over a simulation time of 1,000 τ and 10,000 τ , as shown in

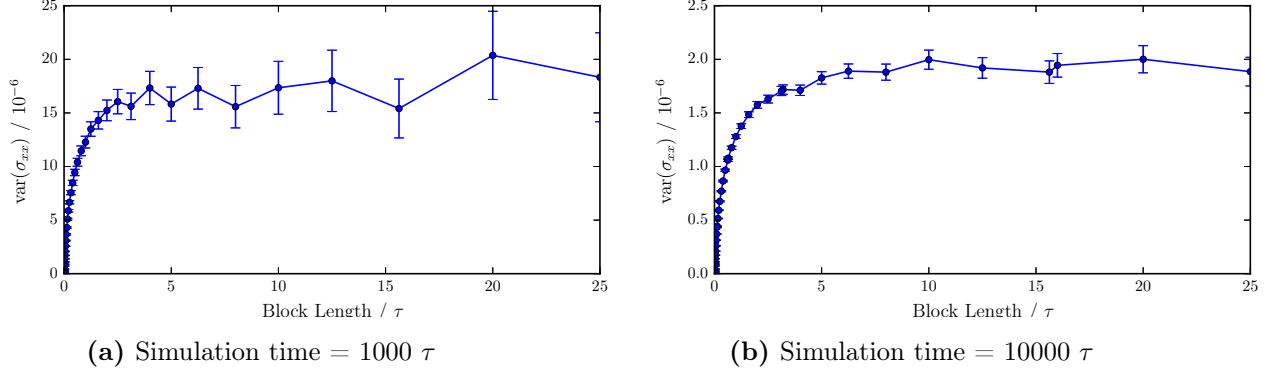


Figure 2: The blocking analysis for a system identical to those studied is compared for simulation times of 1000 τ and 10000 τ . Plateaus in the estimate of the variance begin at block lengths of approximately 5 τ and 10 τ respectively. The error in the variance does not become significant until much larger block lengths. Throughout the subsequent simulations, a block size of 10 τ was used. This ensured decorrelation of the data and produced a reliable estimate of the statistical error.

Figure 2. The plateau begins at a block length of 10 τ for the long simulation and 5 τ for the shorter run, with little increase in the error of the variance until a much larger block size is reached. Consequently, a block length of 10 τ was used to estimate the error of all time-averages calculated in the subsequent simulations.

3.8 Modelling surfactant molecules

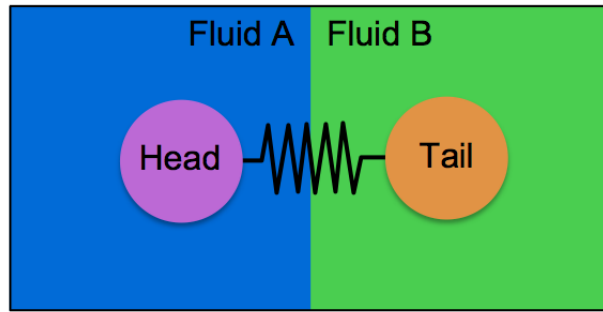


Figure 3: Surfactant molecules were represented by a pair of spherical Lennard–Jones particles connected by a harmonic bond. The head particle has a stronger interaction with Fluid A ($\epsilon_{H,A} = 1.33$ and $\epsilon_{H,B} = 0.17$) whilst the tail has a stronger interaction with Fluid B ($\epsilon_{T,A} = 0.17$ and $\epsilon_{T,B} = 1.33$). This imitates the behaviour of non-ionic surfactant molecules.

To investigate the effects of surfactants on Marangoni flows, surfactant molecules

were modelled as a pair of Lennard–Jones particles connected by a harmonic bond with spring constant $K^* = 25$ and equilibrium bond length $r_0^* = 1.63$. Inspired by Howes and Radke’s study on non–ionic surfactants,⁴⁵ the ‘head’ particle has a stronger interaction with Fluid A particles, ($\epsilon_{H,A} = 1.33$ and $\epsilon_{H,B} = 0.17$) whilst the ‘tail’ particle has a stronger interaction with Fluid B particles ($\epsilon_{T,A} = 0.17$ and $\epsilon_{T,B} = 1.33$). The ‘head’ and ‘tail’ groups interact with each other with strength $\epsilon_{H,T} = 1.00$.

3.9 Software details

All molecular dynamics simulations were run using the LAMMPS package.³³ Additional processing was executed using NumPy.⁴⁶ Graphical figures were plotted using matplotlib.⁴⁷

4 Results and Discussion

4.1 Binary-mixture confined between two walls

Initially, a binary-mixture of two fluids confined between two walls was studied. The fluid was prepared as described in Section 3.5 at a pressure of $P^* = 0.1$ and temperatures of $T^* = 0.8$ and $T^* = 0.9$. The confining walls were used as a piston to control the pressure.

Once equilibrated, the simulations were run for 40×10^6 timesteps of length 0.001τ . The time-averaged number density and virial stress tensor were computed to produce profiles shown in Figures 4 and 5.

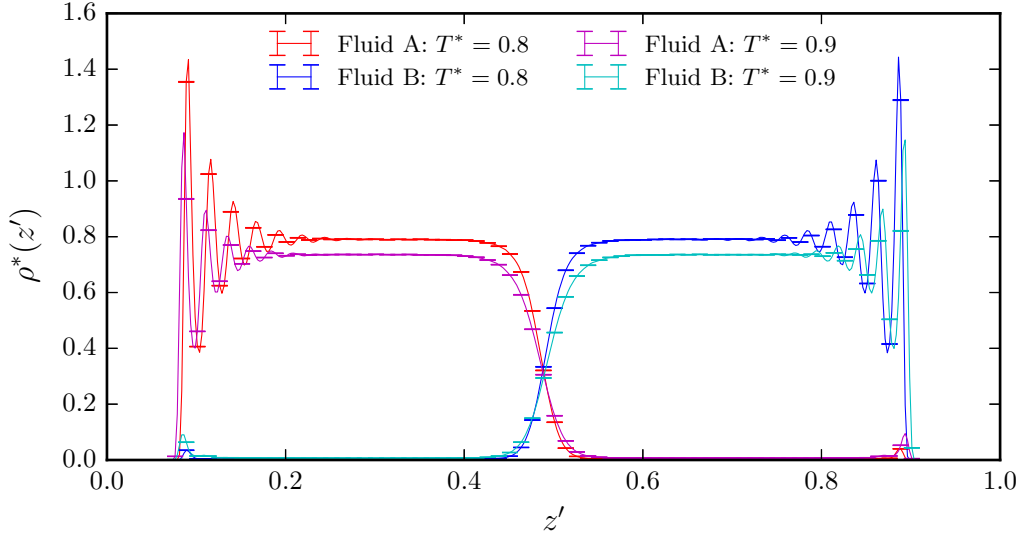


Figure 4: The number density for the two fluids confined between two walls at $T^* = 0.8$ and $T^* = 0.9$ was time-averaged over 40×10^6 timesteps of length 0.001τ . The bulk density is uniform, representing a fluid state, and the interface manifests itself as a sharp change in the densities of the two fluids. Structural layering of the fluid creates oscillations in the density close to the walls.

Both the density and stress profiles show the characteristics expected of a binary-mixture. The bulk density is uniform and there is an interfacial region of where the density of one species falls sharply and the density of the other increases. Close to the walls, there are density oscillations resulting from structural layering of the fluid.

The bulk values for the normal and tangential stress components are equal to $-P_{\text{ext}}$, corresponding to the hydrostatic fluid pressure as expected. There is an

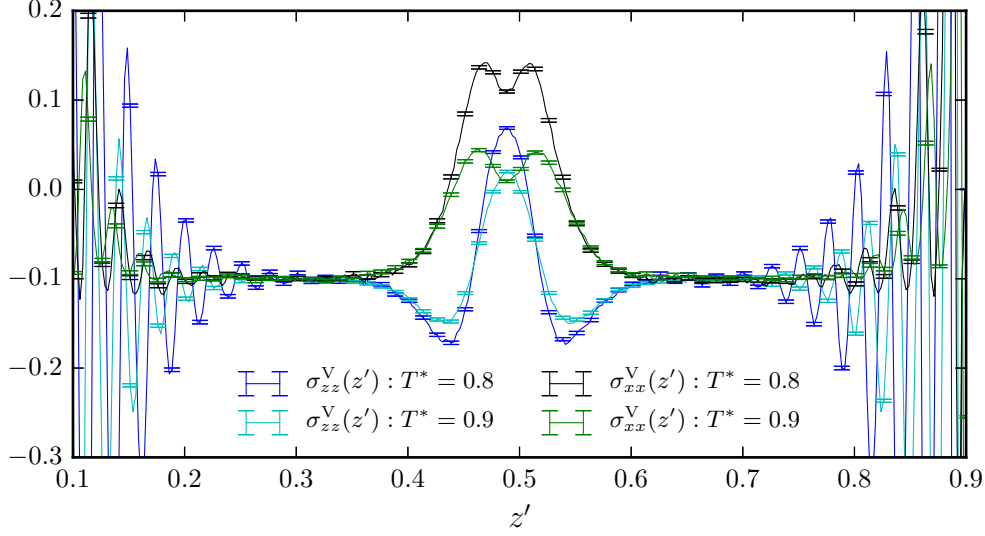


Figure 5: The virial stress tensor components for the combined fluid confined between two walls at $T^* = 0.8$ and $T^* = 0.9$ were time-averaged over 40×10^6 timesteps of length 0.001τ . Both the normal and tangential stress show bulk values equal to $-P_{ext}$, representing the hydrostatic pressure. There is a peak in the tangential stress at the interface due to the anisotropy of the interparticle forces in this region. This can be related to the surface tension and its temperature dependence is the driving force for the Marangoni effect. There is also a change in the normal component at the interface, resulting from the dependence of the virial stress on the local density. Towards the wall there are temperature dependent oscillations in both components, providing the origin of the thermophoretic force.

interfacial peak in the tangential stress due to the anisotropy of the intermolecular forces in this region; this is related to the interfacial tension.⁴⁸ Furthermore, the normal component changes at the interface, resulting from the dependence of the virial stress on density deviations in this region.

The time-averaged values for the stress were then used to estimate the temperature derivative of the tangential stress through Equation 15, as shown in Figure 6. This derivative shows a peak at the interface, providing the origin of the Marangoni force. In the bulk of the fluid the derivative is zero within statistical error, ensuring no force acts this region. In addition, the derivative oscillates at the surface of the wall. This can be interpreted as a thermophoretic force and is henceforth ignored.

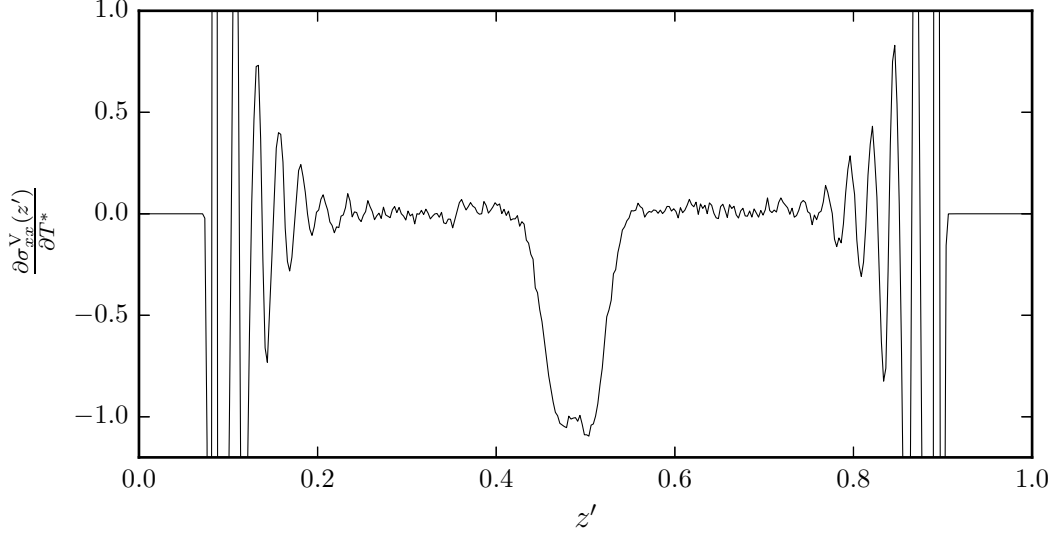


Figure 6: The derivate of the tangential component of the virial stress with respect to temperature was calculated using the finite difference approximation. This shows a negative peak in the interfacial region. When combined with a specified temperature gradient, a force in the opposite direction to a temperature gradient is generated, imitating the Marangoni force. The oscillations at the liquid–solid surface create a thermophoretic force and are subsequently ignored.

Using the central 1/3 of the derivative profile and a temperature gradient of $\partial T^*/\partial x^* = 0.001$, an artificial Marangoni force was computed through Equation 14. This force was applied to an identical system prepared at $T^* = 0.85$. An equilibrium simulation was then run for 40×10^6 timesteps, and the time-average of the x-component of the fluid velocity $v_x^*(z')$ was computed. The momenta of the walls in the x, y plane were fixed to provide a stationary reference point, creating a momentum sink.

The velocity profile is shown in Figure 7. There is a sharp negative peak at the interface indicating a Marangoni flow in the opposite direction to the temperature gradient. Furthermore, the flow decays linearly away from the interface, consistent with a Couette flow arising from shear-driven fluid motion.⁴⁹

There is also a net flow in the system, suggesting an overall force acting on the fluid. The walls provide a frictional force which allows this steady-state flow to arise under the isolated effect of a temperature-gradient.

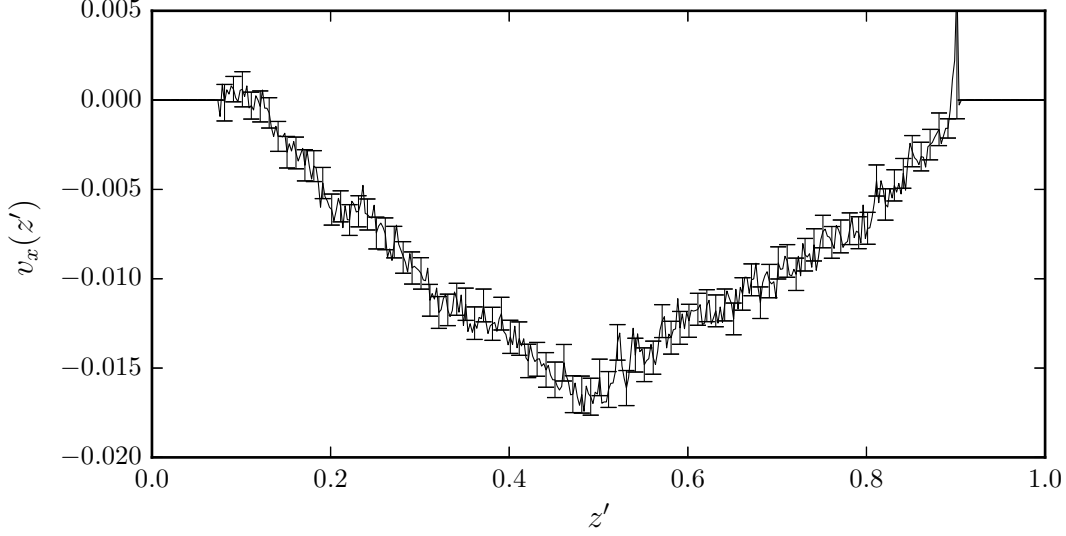


Figure 7: The velocity profile of a confined fluid at $T^* = 0.85$ with an applied force calculated from Figure 6 was time-averaged over 40×10^6 timesteps of length 0.001τ . A steady state negative interfacial peak emerges, corresponding to a Marangoni flow in the opposite direction to the temperature gradient. This peak decays linearly to zero at the surface of the bounding walls, corresponding to a Couette flow.

4.1.1 Comparing to the Irving–Kirkwood stress

Figure 5 shows the normal component of the virial stress is not uniform across the interface. In contrast, the normal component of the Irving–Kirkwood stress does not depend on the local fluid density and should be constant throughout the liquid. To verify if the difference in these methods is significant for the measurement of Marangoni forces, the Irving–Kirkwood stress was also calculated.

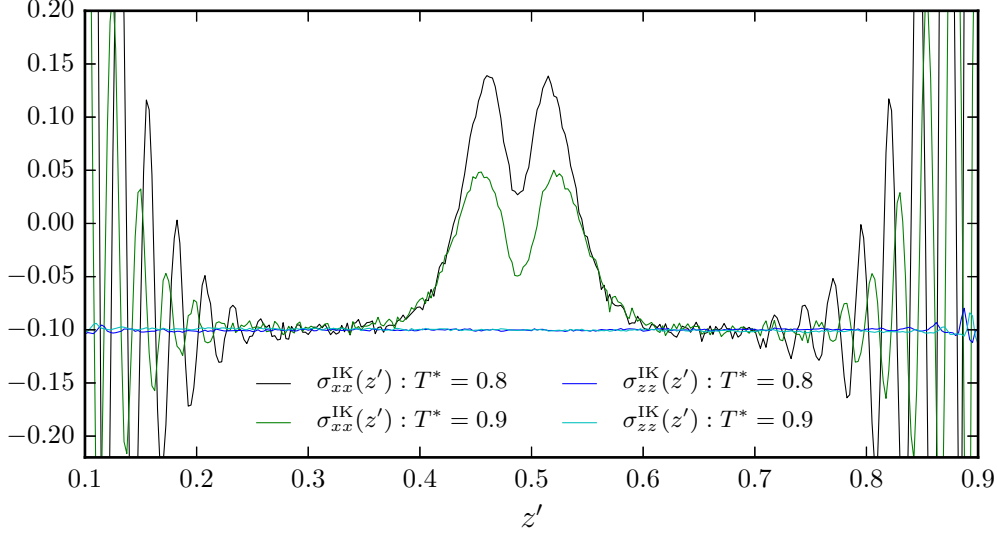


Figure 8: The Irving–Kirkwood stress tensor components for the combined fluid confined between two walls at $T^* = 0.8$ and $T^* = 0.9$ were time-averaged over 1×10^6 timesteps of length 0.001τ . Both the normal and tangential stress show bulk values equal to $-P_{ext}$, representing the hydrostatic pressure. Similar to Figure 5, there is a peak in the tangential stress at the interface due to the anisotropy of the interparticle forces in this region. However, this peak is divided into two with a reduction in the stress directly at the interface. This difference to the virial stress arises because the Irving–Kirkwood stress does not depend on the local density. The normal components of the stress are constant across the system, as expected.

The fluids were prepared at $P^* = 0.1$ and $T^* = 0.8$ and $T^* = 0.9$ as before. Since the Irving–Kirkwood stress tensor was more computationally expensive (see Section 3.6), the equilibrium simulations were only run for 1×10^6 timesteps, resulting in a greater amount of statistical error. The time-averaged stress is plotted in Figure 8. The tangential component shows a similar profile to the virial stress, although the interfacial peak is divided into two with a reduction in the stress directly at the interface. This difference directly at the interface arises since the Irving–Kirkwood does not depend on local density. The normal component of the Irving–Kirkwood stress is uniform, representing the isotropy of the system in this direction.

The finite difference method was again used to calculate the temperature derivative of the stress, and this is compared to the virial result in Figure 9. Still focussing on the central $1/3$ of the fluid, there is a good correspondence between the two derivatives and the interfacial peak occurs across the same spatial region and with the same maximum value. The most significant difference appears directly at the

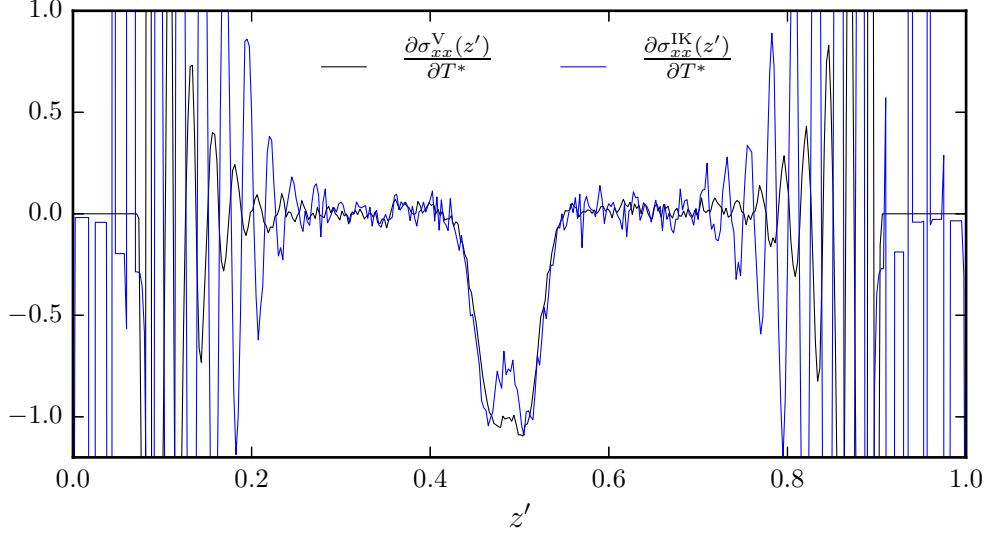


Figure 9: The derivate of the tangential component of the Irving–Kirkwood stress with respect to temperature was calculated using the finite difference approximation. There is an analogous negative peak in the interfacial region to Figure 6, with a similar magnitude and spatial extent. However, the peak in the Irving–Kirkwood derivative is split into two. This difference arises because, unlike the virial stress, the Irving–Kirkwood stress does not depend on local density. When combined with a specified temperature gradient, a force in the opposite direction to a temperature gradient is generated, imitating the Marangoni force. The derivative in the bulk is zero, providing no body force acting on the fluid away from the interface.

interface, where there is a sharp reduction in the derivative of the Irving–Kirkwood stress. This is probably a result of the reduction in density at the interface affecting the virial and not the Irving–Kirkwood stress.

Using a temperature gradient of $\partial T^*/\partial x^* = 0.001$ to compute the Irving–Kirkwood artificial body force, an equilibrium simulation at $T^* = 0.85$ was run for 40×10^6 timesteps. The fluid velocity was measured and compared to the result obtained using the virial force, as shown in Figure 10. The profiles show a close correspondence, especially for the region $z' \leq 0.4$, although they deviate for higher values of z' . In particular, the flow from the Irving–Kirkwood method is smaller directly at the interface, due to the reduction in the force at this point. The Irving–Kirkwood velocity is also asymmetric despite the symmetry of the system. This may be the result of the increased noise in the Irving–Kirkwood force relative to the virial force, resulting from the shorter simulation time enforced by the high computational cost of the Irving–Kirkwood analysis.

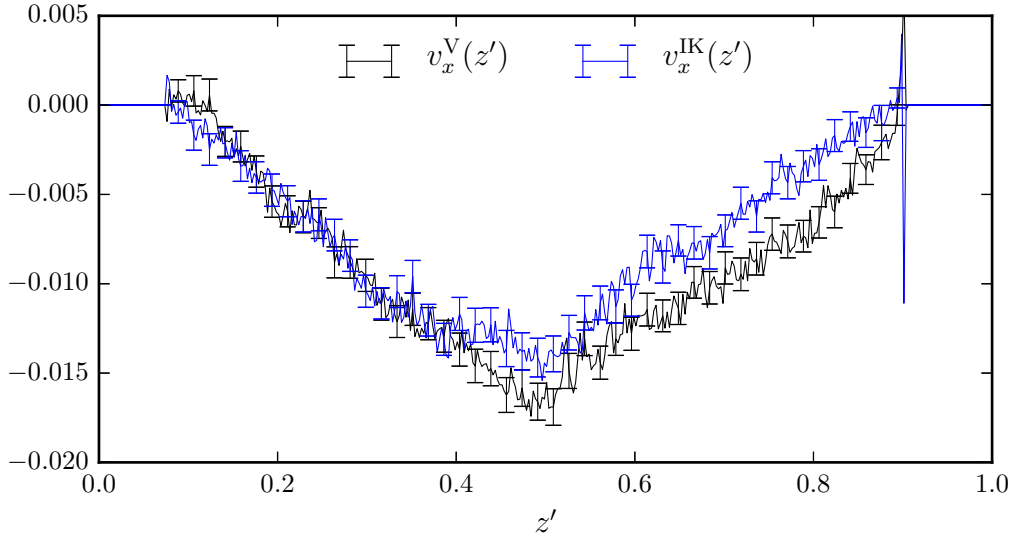


Figure 10: The velocity profile of a confined fluid at $T^* = 0.85$ with an applied force calculated from Figure 9 was time-averaged over 40×10^6 timesteps of length 0.001τ . This is compared to the velocity profile produced using the force calculated from the virial stress. Both show a steady state negative interfacial peak, corresponding to a Marangoni flow in the opposite direction to the temperature gradient, with a linear decay into the bulk. The peak value using the force calculated from the Irving–Kirkwood stress is not as large as that using the force calculated from the virial stress. This is a result of the reduction of the Irving–Kirkwood stress derivative directly at the interface. Moreover, the virial flow is symmetric about the interface whilst the Irving–Kirkwood flow is not. This is probably a result of the increase in noise in the Irving–Kirkwood derivative due to a shorter simulation time.

4.2 Binary–mixture periodic in 3-dimensions

Equation 1 demonstrated that a temperature gradient in a system cannot generate a net fluid flow. Levich described how the interfacial flow must be accompanied by a back-flow in the bulk.⁴ For the binary–mixture held between two walls, the walls provide a momentum sink allowing a net flow to exist within the fluid. To replicate the behaviour of an infinite fluid where a back flow may be observed, a system void of momentum sinks must be studied. For example, a binary–mixture of two partially miscible fluids with periodic boundary conditions in all dimensions can be used.

This system, shown in Figure 1a, was prepared as described in Section 3.5 with the parameters given in Section 3.1. The distance between consecutive interfaces was $0.5L_{z^*}$. A Nosé–Hoover barostat and thermostat were used to regulate the pressure at $P^* = 0.1$ with temperatures of $T^* = 0.8$ and $T^* = 0.9$.

4.2.1 Comparing the virial and Irving–Kirkwood stress

Again there is an ambiguity over which stress tensor should be used to compute the Marangoni force. Once equilibrated, the system was simulated for 10×10^6 timesteps over which the number density, virial and Irving–Kirkwood stress were computed. The Irving–Kirkwood analysis was computationally expensive and this was the longest feasible simulation length.

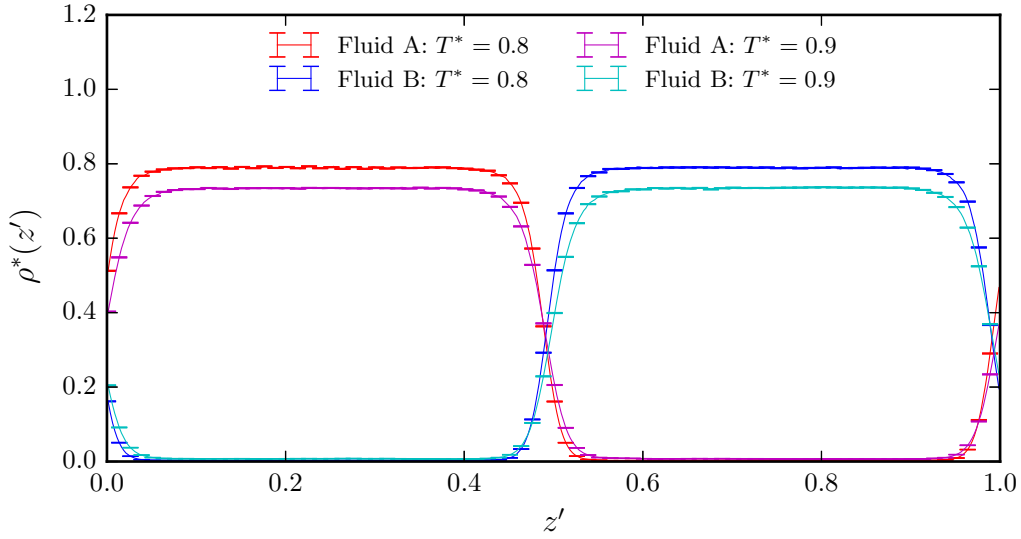


Figure 11: The number density for the two fluids periodic in all dimensions at $T^* = 0.8$ and $T^* = 0.9$ was time-averaged over 10×10^6 timesteps of length 0.001τ . The bulk density is uniform, representing a fluid state, and the interfaces manifest themselves as a sharp change in the densities of the two fluids. Between the two temperatures the position of the interface is slightly shifted, this must be corrected before calculating the stress derivative.

The resulting density profile plotted in Figure 11 showed a uniform bulk density and a sharp interfacial region as expected. However, the position of the interface shifted during the simulation and was no longer coincident for the two temperatures. Recentering the interfaces removed this shift before calculating the Marangoni force.

The recentered virial and Irving–Kirkwood stress components are plotted in Figures 12 and 13 respectively. As with the confined fluid, the bulk stress components are equal to $-P_{\text{ext}}$, corresponding to the hydrostatic fluid pressure. There is an interfacial peak in both the virial and Irving–Kirkwood tangential stress at the interface with a similar maximum value, although the Irving–Kirkwood stress shows a stronger minimum directly at the interface. Similar to Figure 8, this is probably the

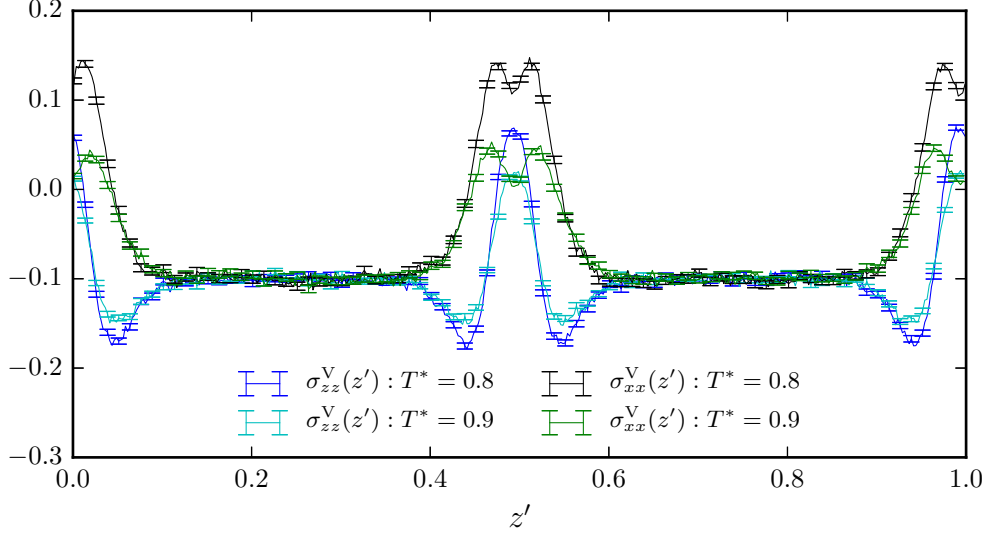


Figure 12: The virial stress tensor components for the combined fluid periodic in all dimensions $T^* = 0.8$ and $T^* = 0.9$ were time-averaged over 10×10^6 timesteps of length 0.001τ . Both the normal and tangential stress show bulk values equal to $-P_{ext}$, representing the hydrostatic pressure. There is a peak in the tangential stress at the interface due to the anisotropy of the interparticle forces in this region. This peak has a similar form to that seen in Figure 5, and its temperature dependence provides the origin of the Marangoni effect. There is also a change in the normal component at the interface, resulting from the dependence of the virial stress on density deviations.

result of a reduced density in the interfacial region. Furthermore, the normal component of the Irving–Kirkwood stress is uniform across the interface, as expected.

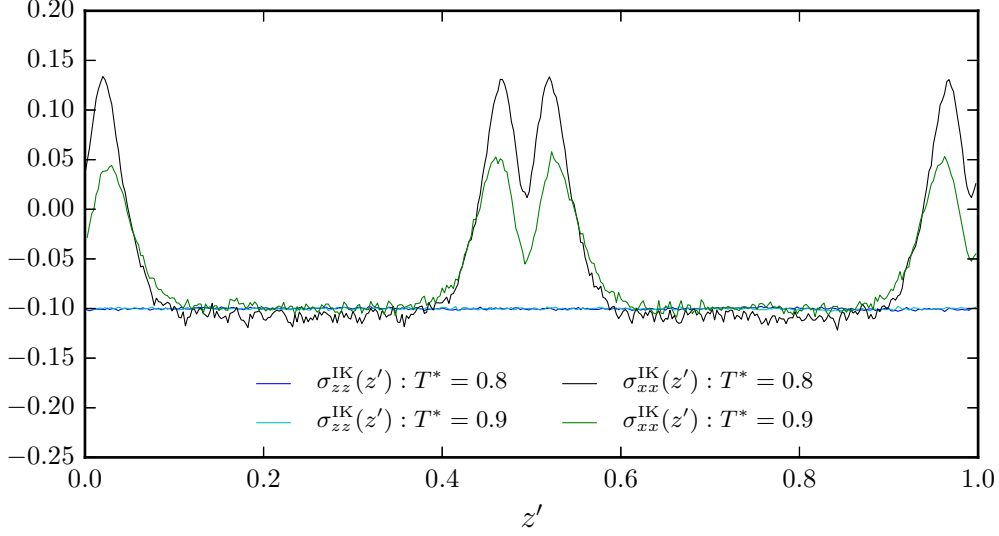


Figure 13: The Irving–Kirkwood stress tensor components for the combined fluid periodic in all dimensions $T^* = 0.8$ and $T^* = 0.9$ were time-averaged over 10×10^6 timesteps of length 0.001τ . Both the normal and tangential stress show bulk values equal to $-P_{ext}$, representing the hydrostatic pressure. There is a peak in the tangential stress at the interface due to the anisotropy of the interparticle forces in this region. This peak has a similar form to that seen in the virial stress, although they deviate directly at the interface. Since the Irving–Kirkwood stress does not depend on local density, the normal component is uniform across the system, as expected.

The temperature derivative of the tangential stress was calculated through the finite difference approach. The derivative profile was adjusted by subtracting the average from each value, ensuring the integral over all space was zero, as shown in Figure 14. This guaranteed there would be no net force applied to the fluid, even in the absence of a momentum sink.

The derivative profile shows a similar interfacial peak to Figure 9. The maximum values are similar, suggesting that fixing the total force to zero correctly adjusts the derivatives to give a physically meaningful Marangoni force. There is a good correspondence between the derivatives calculated from the Irving–Kirkwood and virial stress tensors, although the magnitude of the Irving–Kirkwood peak is reduced directly at the interface. In the bulk fluid, the derivative opposes the interfacial peak, generating the back force which balances the Marangoni force. However, the profile shows too much noise for determination of the fine-structure and is not of sufficient quality for calculating an artificial body-force.

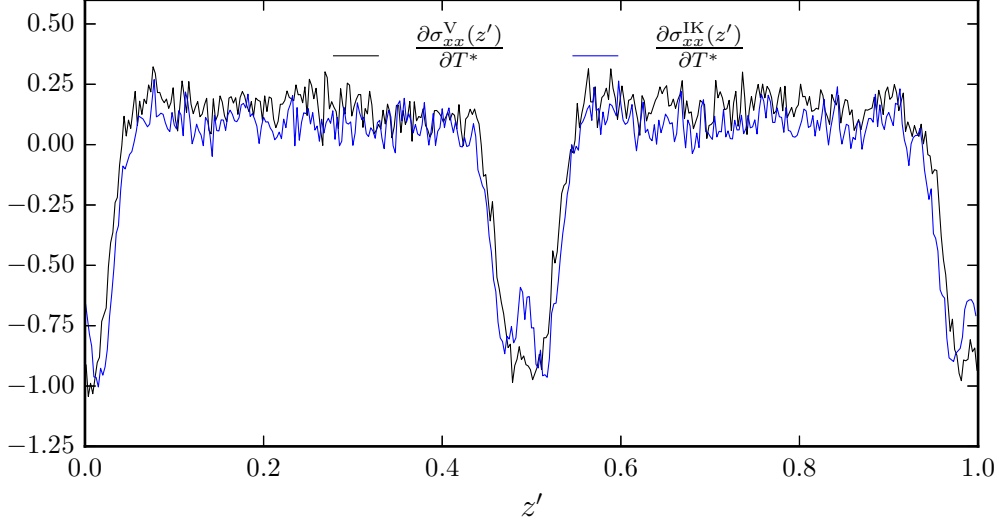


Figure 14: The derivate of the tangential component of the Irving–Kirkwood and virial stress with respect to temperature was calculated using the finite difference approximation. The average value was subtracted to ensure the integral of the derivative profile over all space was zero. Both the virial and Irving–Kirkwood stress derivatives show a negative peak at the interface, with a similar maximum value and spatial extent. However, there is too much noise in these profiles, obscuring the fine structure and preventing a definitive comparison. Furthermore, these derivatives are not precise enough to be useful for calculating an artificial body force.

4.2.2 Reducing the noise in the force–profile

To generate a profile with reduced noise requires either a larger system or a longer simulation time. Both of these increase the computational cost of calculating the Irving–Kirkwood stress beyond a practical level, and only the virial stress can be used. Considering how similar the virial and Irving–Kirkwood derivative profiles appear in Figure 9, using the virial stress does not create too much deviation from the more suitable Irving–Kirkwood stress, whilst enabling a much longer simulation time.

The reduced noise stress was calculated by running the equilibrium systems for 30×10^6 timesteps. Recentering the interfaces generated the virial stress shown in Figure 15. For both temperatures, the profiles show much less noise compared to Figure 12, especially in the bulk region, and the interfacial peaks are more symmetric.

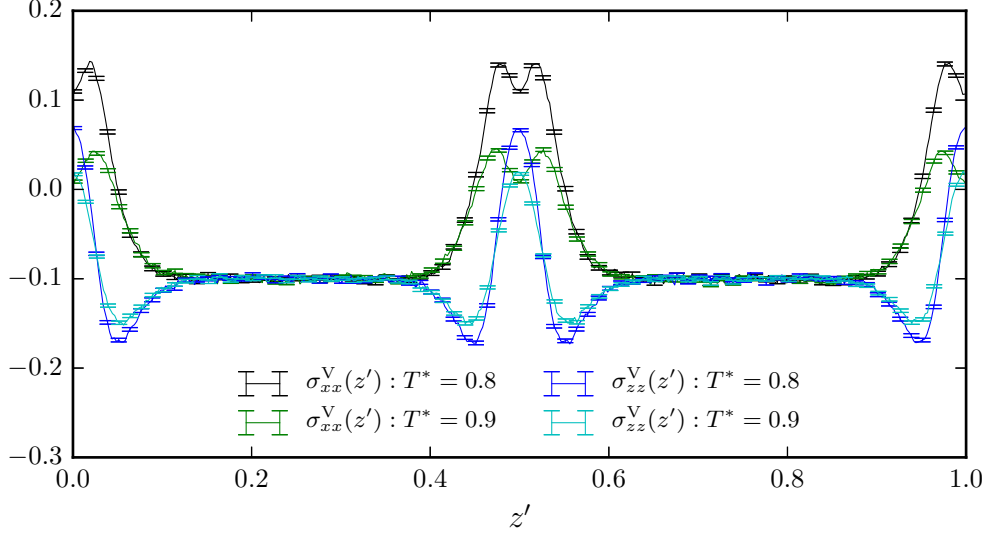


Figure 15: The virial stress tensor components for the combined fluid periodic in all dimensions $T^* = 0.8$ and $T^* = 0.9$ were time-averaged over 30×10^6 timesteps of length 0.001τ . This produced a significant reduction in noise relative to Figure 12. As before, both the normal and tangential stress show bulk values equal to $-P_{ext}$, representing the hydrostatic pressure. There is a peak in the tangential stress at the interface due to the anisotropy of the interparticle forces in this region. The normal component at the interface also deviates from the bulk value as a result of the dependence of the virial stress on the local density.

The temperature derivative of the tangential stress was again computed using the finite difference and the average value subtracted to give the profile shown in Figure 16. There is a dramatic reduction in the noise compared to Figure 14, with a peak at the interface and an opposing derivative in the bulk regions.

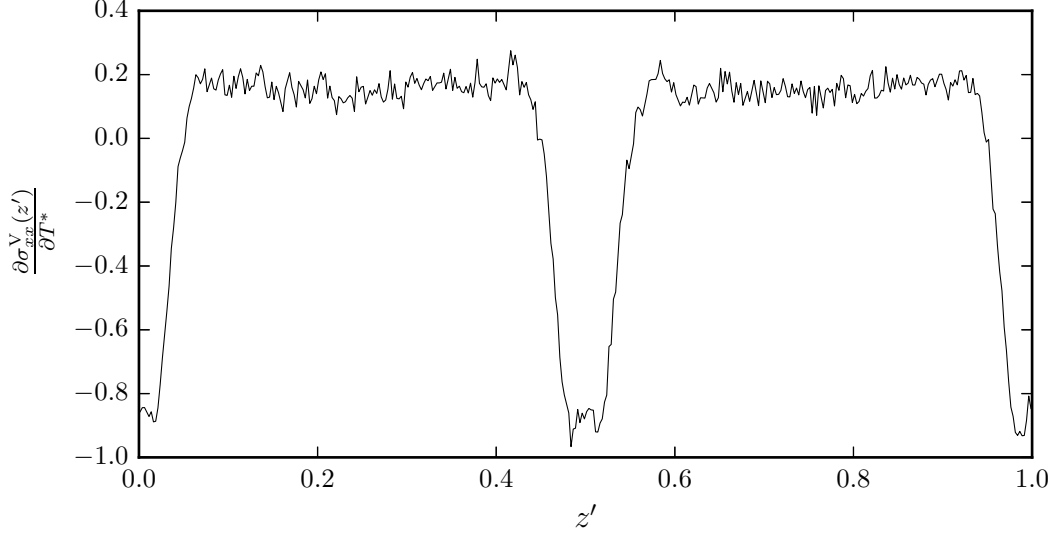


Figure 16: The derivate of the tangential component of the virial stress was calculated using the finite difference approach. The average value was subtracted to ensure the integral of the derivative profile over all space was zero. There is a significant reduction in noise compared to Figure 14. A sharp, negative peak can be seen at the interface, leading to the Marangoni force, and an opposing derivate occurs in the bulk of the fluid, yielding a balancing back flow.

Using the stress derivative given in Figure 16 and a temperature gradient of $\partial T^*/\partial x^* = 0.001$, an artificial body force was computed. This force was applied in an equilibrium simulation at $T^* = 0.85$ and run for 40×10^6 timesteps. The time-averaged velocity $v_x^*(z')$ was computed to give the profile plotted in Figure 17.

Despite the stress derivative being adjusted to remove any net force, the velocity profile shows a net centre-of-mass motion (indicated by the hashed line). It is possible that this motion could arise from errors due to the linear approximation used to calculate the Marangoni force. This may be due to the use of too large a temperature difference. Repeating the simulations using temperatures of $T^* = 0.7$ and $T^* = 0.9$ produced an even larger centre-of-mass motion, supporting this explanation. It is unlikely that in the absence of a momentum sink for a system like this, the net flow could be removed without artificially fixing the centre-of-mass throughout the simulation.

Despite this, it may be possible to consider the relative motion across the fluid, and this does appear to show a negative Marangoni flow at the interfaces (with $v < v_{\text{COM}}$) and a back flow in the bulk fluid (with $v > v_{\text{COM}}$) as expected. This conclusion is, however, somewhat ambitious and there was insufficient time to improve the

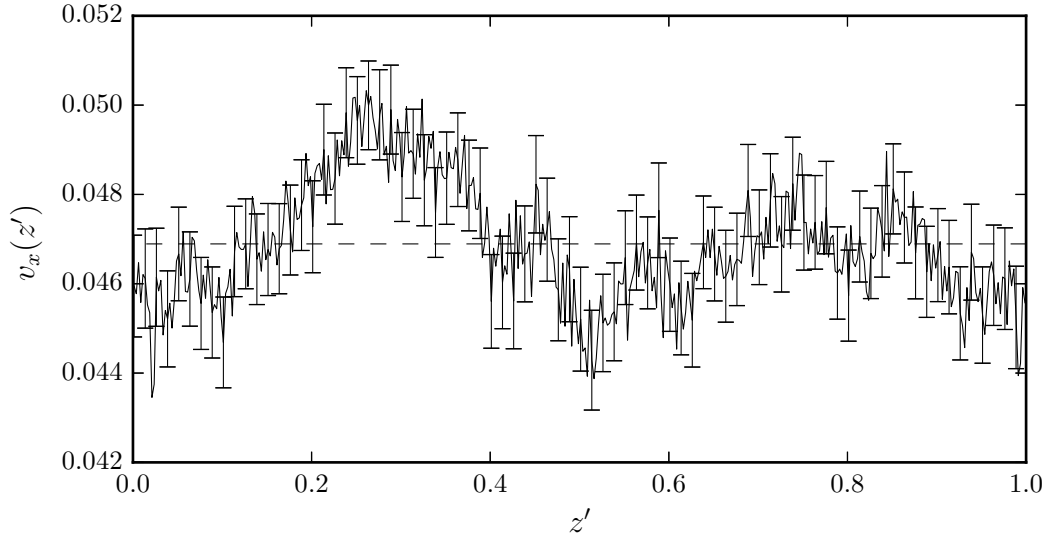


Figure 17: The velocity profile of an infinite binary-mixture at $T^* = 0.85$, with an applied force calculated using Figure 16 and temperature gradient of $\partial T^*/\partial x^* = 0.001$, was time-averaged over 40×10^6 timesteps of length 0.001τ . A non-equilibrium emerges with a non-zero average velocity (indicated by the hashed line), despite the average derivative being fixed to zero. It is unlikely this could be removed without artificially fixing the centre-of-mass. Despite this, the fluid velocity relative to this centre-of-mass motion may suggest a Marangoni flow at the interfaces with an opposing flow in the bulk regions, as predicted by Levich.⁴

simulation further.

4.3 The effect of surfactants

Surfactant molecules decrease surface tension as they have a favourable interaction with both fluids and bridge the interfacial plane. This should also decrease a surface tension gradient and reduce the Marangoni effect, as observed experimentally.^{22–25}

The non-ionic surfactant molecules described in Section 3.8 were added to the binary-mixture confined between two walls. This system was chosen since Section 4.1 showed it allowed a steady-state flow to be modelled effectively.

The surfactant molecules were added to a single plane between the two fluids in the initial lattice before melting. A certain fraction of these molecules were then removed to vary the surfactant concentration, quantified as a fraction of the total number of particles present,

$$\text{Surfactant Fraction} \equiv \frac{N_{\text{surfactant}}}{N_{\text{surfactant}} + N_{\text{fluid}}}. \quad (32)$$

This allowed the surfactant fraction to be varied between 0 and 0.0323.

Taking fractions of 0.000, 0.0031, 0.0098, 0.0194, 0.0264, 0.0298 and 0.0323, the fluid was prepared as described in Section 3.5, with a pressure of $P^* = 0.1$ and temperatures of $T^* = 0.8$ and $T^* = 0.9$. A piston barostat and Nosé–Hoover thermostat were used and each system was run at equilibrium for 30×10^6 timesteps of length 0.001τ .

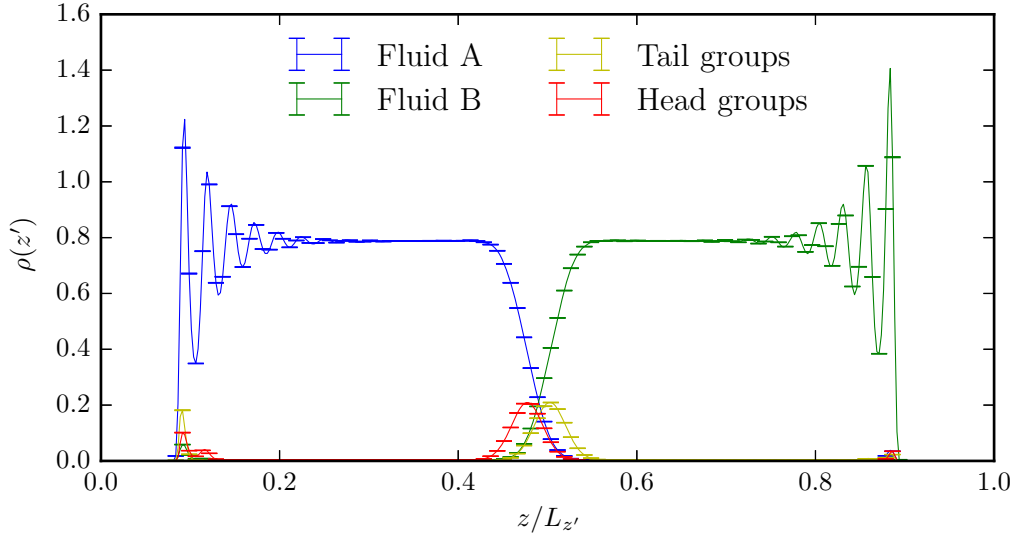


Figure 18: The number density for the confined binary-mixture with a non-ionic surfactant fraction of 0.0194, pressure of $P^* = 0.1$ and at $T^* = 0.8$ was time-averaged over 30×10^6 timesteps of length 0.001τ . There is a uniform density in the bulk, and an interface represented by a sharp change in the densities of Fluid A and Fluid B. The surfactant particles are localised at the interface with a low solubility. They show the correct orientation, with ‘Head’ particles interacting most strongly with Fluid A and ‘Tail’ particles with Fluid B.

The number density of each species shows a uniform bulk density, a sharp interface and peaks for the head and tail groups located at the interface, as shown for $T^* = 0.8$ and a surfactant fraction of 0.0194 in Figure 18. The surfactant molecules were correctly oriented with head groups interacting with Fluid A and tail groups with Fluid B.

The virial stress used to compute the temperature derivative of the tangential stress for each surfactant fraction. These results, plotted in Figure 19, show a reduction in the magnitude of the interfacial peak as the surfactant fraction increases, corresponding to a reduction in the Marangoni force.

Two smaller positive peaks on either side of the centre also develop for higher

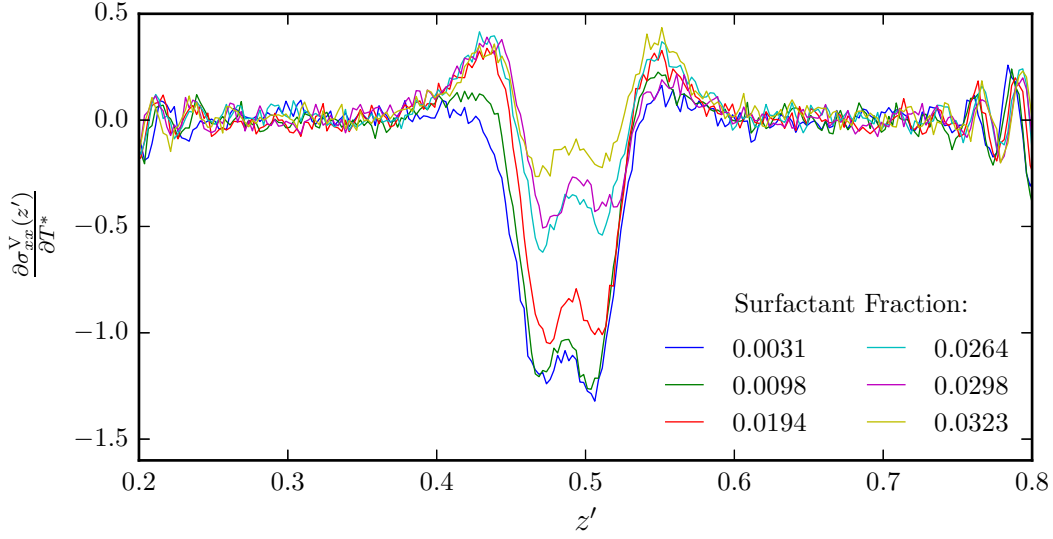


Figure 19: The derivative of the tangential component of the virial stress with respect to temperature was calculated for a range of surfactant fractions using the finite difference approximation. For a low surfactant fraction, there is strong interfacial peak providing the origin of the Marangoni force. As the amount of surfactant is increased, the strength of this peak decreases to zero indicating the eradication of the Marangoni effect. Two smaller positive peaks on either side of the centre also develop for higher surfactant fractions. This probably results from an increase in the number density in this region, due to localisation of the surfactant particles at the interface.

surfactant fractions. These may be the result of an increase in the local density, due to localisation of the surfactant particles in this region and the density dependence of the virial stress. An increase in surfactant fraction would exaggerate this density change. This could be verified by computing the Irving–Kirkwood stress, where any peaks due to density deviations should disappear.

Furthermore, the harmonic forces in the surfactant molecules could contribute to these peaks. This could be investigated by varying the spring constant for the surfactant bond.

Using a temperature gradient of $\partial T^*/\partial x^* = 0.001$, the central 1/3 of the stress derivative profiles in Figure 19 were used to compute an artificial body force, which was applied to simulations at $T^* = 0.85$. These were run for 30×10^6 timesteps over which $v_x(z')$ was measured and plotted in Figure 20. The interfacial velocity decreases as the surfactant fraction is increased, suggesting a surfactant induced retardation of the Marangoni flow.

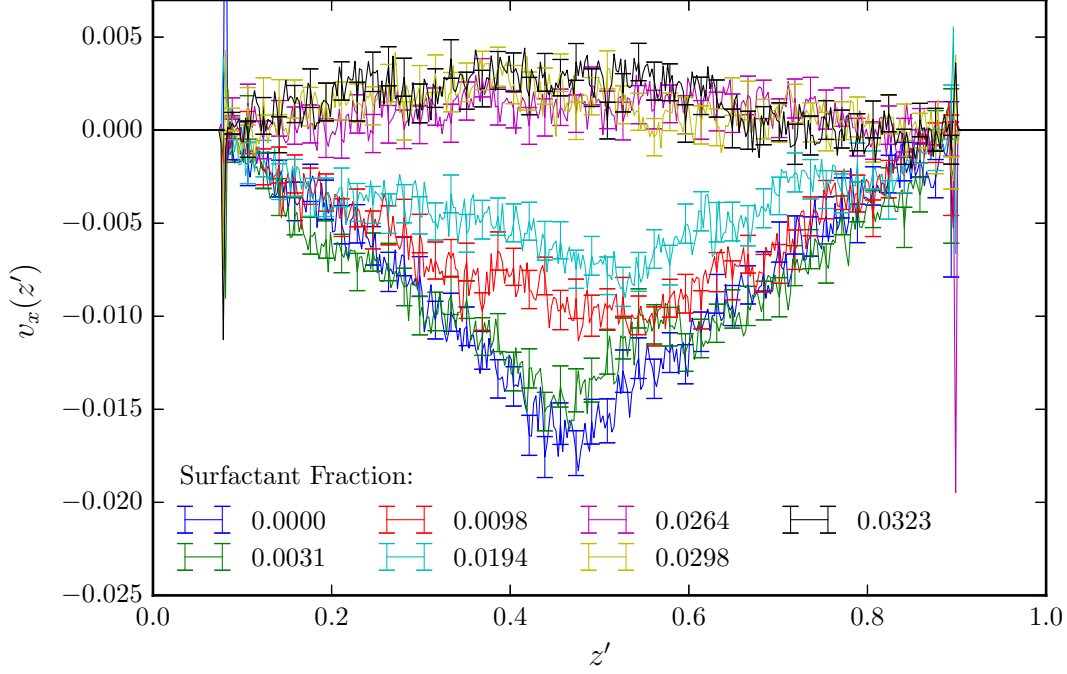


Figure 20: The velocity profile of an confined binary-mixture at $T^* = 0.85$, with an applied force calculated using Figure 19 and temperature gradient of $\partial T^*/\partial x^* = 0.001$, was time-averaged over 40×10^6 timesteps of length 0.001τ for a range of surfactant fractions. For a low surfactant fraction, the flow profile closely resembles that of the non-surfactant system (Figure 7, with a negative interfacial peak and a linear decay into the bulk. As the amount of surfactant increases there is a reduction in the magnitude of this peak until the Marangoni flow essentially disappears. Moreover, the peak becomes less sharp at higher surfactant fractions. This is probably due to the non-uniform viscosity created by the added surfactant molecules.

Comparing the peak value of the flow velocity against the surfactant fraction shows a reduction in the peak magnitude as the surfactant fraction increases, as shown in Figure 21. Above a fraction of 0.025 the Marangoni effect has effectively been removed. This retardation has been observed experimentally by Barton and Subramanian, and is discussed in their study on the relation between droplet size and motion under a vertical temperature gradient.²⁴ They note that droplets sink on the addition of a non-ionic surfactant, indicating the eradication of the Marangoni force and the dominance of gravity.

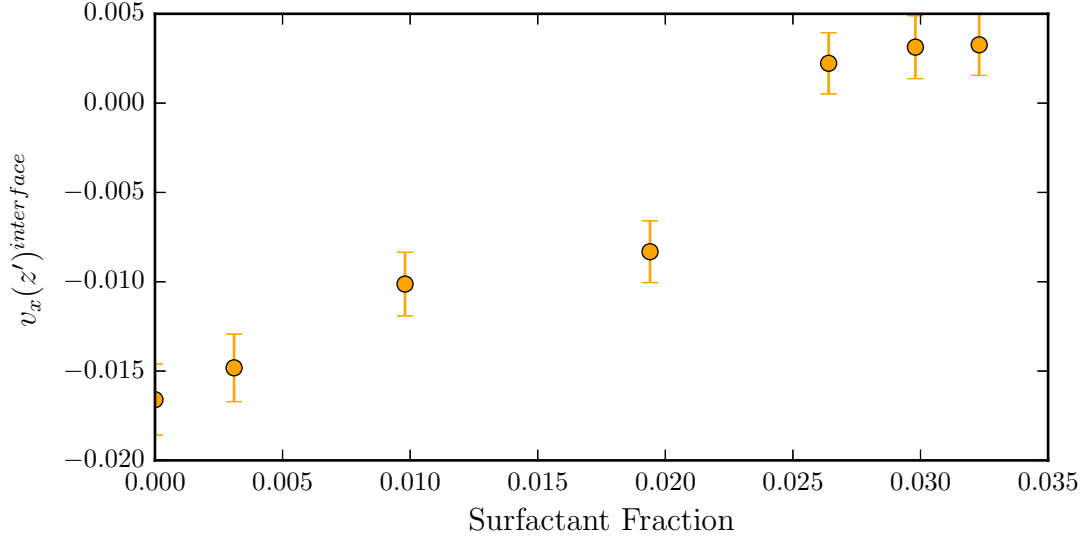


Figure 21: Comparing the surfactant fraction to the interfacial velocity demonstrates the retardation of the Marangoni flow in the presence of surfactant molecules. Above a fraction of 0.025, this velocity is essentially zero, although there is small velocity in the opposite direction to the Marangoni flow. This may be the result of the secondary peaks that emerge in Figure 19 which only become significant for high surfactant fractions.

The sharpness of the Marangoni flow peak in Figure 20 also decreases as the surfactant fraction increases and no longer fits the Couette model as conclusively. This may be due to a reduction in viscosity at the interface from the presence of surfactant molecules, giving a non-uniform viscosity across the fluid. To confirm this, the viscosity could be measured using the Green–Kubo relation,

$$\eta = \frac{1}{Vk_{\text{B}}T} \int_0^\infty \langle \sigma_{xy}(\tau) \sigma_{xy}(0) \rangle d\tau. \quad (33)$$

5 Concluding Remarks

Using equilibrium simulations at two close temperatures, the temperature derivative of the tangential stress was estimated for binary-mixtures through a finite-difference method. The derivatives of the virial and Irving-Kirkwood stresses were calculated for a mixture confined between two walls, and in both cases there was a similar negative interfacial peak. Combining with a temperature gradient, an artificial body force was computed and applied in a third equilibrium simulation, resulting in a non-equilibrium with a net interfacial flow. This was interpreted as a Marangoni flow and occurred in the opposite direction to the applied temperature gradient, as expected. The confining walls provided a momentum sink, exerting a frictional force on the fluid and allowing a steady state flow to be achieved.

The same method was then applied for a binary-mixture periodic in all dimensions, and a similar peak in the stress derivative was observed. However, the fine structure of this derivative was obscured by significant noise. This was reduced by running the simulation for a longer time period. Consequently, only the virial stress was feasible for calculating a sufficiently precise gradient profile.

In the absence of a momentum sink, the stress derivative was adjusted to ensure no net force was applied on the system, and was used to calculate an artificial body force. Applying this force produced a flow profile with a net centre-of-mass motion despite the adjustment applied to remove a net force.

The origin of the centre-of-mass motion is unclear. It could arise from errors induced by noise in the applied force. For example, errors in the average derivative will cause the derivative profile to be incorrectly recentred, and a net applied force could result. Running the initial equilibrium simulations for an even longer period could allow the effect of noise to be verified.

Alternatively, the centre-of-mass could be artificially fixed throughout the simulation. However, observing a stationary centre-of-mass is essential to verifying the correct behaviour of Marangoni flows, and fixing the centre-of-mass would obscure this. Fixing the centre-of-mass would allow only the relative motion of different fluid regions to be observed.

Having established an effective model using the fluid confined between two walls, the effect of surfactants was investigated by adding different concentrations of non-ionic surfactant molecules into the interfacial region. The tangential virial stress was computed at two temperatures and its temperature derivative was estimated through the finite difference. As the concentration of surfactant increased, the magnitude

of the negative interfacial peak was reduced and two secondary positive peaks on either side of the interface emerged.

The stress derivatives were used to calculate an artificial body force that was applied in a third equilibrium simulation. The magnitude of the resulting Marangoni flow decreased to zero as the surfactant concentration increased, in agreement with experimental studies. Furthermore, the shape of the velocity profile deviated from the linear decay observed in the absence of surfactant. This may be due to a non-uniform fluid viscosity, since the addition of surfactants should decrease the viscosity of the interfacial region.

5.1 Future directions of study

There are a number of ambiguities in the results reported which further study could verify. For example, more accurate force profiles from the Irving–Kirkwood stress could be computed using a larger system. This could be made more efficient by implementing the Irving–Kirkwood analysis in parallel.

Furthermore, by introducing a contribution from the harmonic bonding into the Irving–Kirkwood analysis, it could be used to study systems with added surfactant. This would confirm whether the secondary peaks observed as surfactant fraction increases are the result of an increase in local density due to the presence of surfactant particles.

It would also be interesting to compute the viscosity across the liquid and compare this for the pure fluid and the fluid with surfactant present. As described in Section 4.3, this can be calculated using a Green–Kubo relation. Comparing the shape of the flow profile to the uniformity in the viscosity would allow the deviation from the Couette flow model to be investigated.

Beyond this, linear response theory suggests that the flow induced by a temperature gradient could be computed as:

$$\langle v_x \rangle = \frac{\nabla T}{T} V \int_{\tau=0}^{\infty} \langle J_x(0) Q_x(\tau) \rangle d\tau, \quad (34)$$

where J and Q are the mass and heat flux respectively. By computing this average velocity for the mixture confined between two walls, both with and without an applied body force, Equation 34 could allow a general relation between flow velocity and a temperature gradient to be developed. This could be compared for the bulk and interfacial regions, since there should be no correlation between the heat flux and mass flux away from the interfaces.

Furthermore, a greater understanding could be developed using Onsager's reciprocal rule, as employed by Derjaguin et al. This could be achieved by applying a pressure gradient to a simulation and measuring the resulting heat flux. From the relation of these quantities, the mass flux from a temperature gradient could be computed.

Finally, once informative methods for the basic study of Marangoni flows have been developed, the natural progression would be to investigate different systems and geometries. For example, it would be interesting to study a non-symmetric binary-mixture or to replicate the thermophoresis of droplets under a temperature gradient, as observed experimentally.

Through the results of this study, combined with future work, a greater understanding of the relationship between the stresses within a fluid and the velocity due to a temperature gradient can be achieved. Ultimately this is working towards a microscopic description and a more comprehensive understanding of the Marangoni effect.

References

1. J. THOMPSON, *Phil. Mag.* **10**, 330 (1855).
2. C. MARANGONI, *Ann. der Phys* **22**, 337 (1871).
3. B. V. DERJAGUIN, N. V. CHURAEV, and V. M. MULLER, *Surface Forces*, Consultants Bureau, 1987.
4. V. G. LEVICH, *Physiochemical Hydrodynamics*, Prentice–Hall, 1962.
5. J. L. ANDERSON, *Ann. Rev. Fluid Mech.* **21**, 61 (1989).
6. R. CINI, G. LOGLIO, and A. FICALBI, *J. Colloid Interface Sci.* **41**, 287 (1972).
7. W. V. KAYSER, *J. Colloid Interface Sci.* **56**, 622 (1975).
8. H. A. MAIER, P. A. BOPP, and M. J. HAMPE, *Can. J. Chem. Eng.* **90**, 833 (2012).
9. D. C. VENERUS and D. N. SIMAVILLA, *Scientific Reports* **5**, 16162 (2015).
10. R. TADMOR, *J. Colloid Interface Sci.* **332**, 451 (2009).
11. R. VUILLEUMIER, V. EGO, L. NELTNER, and A. M. CAZABAT, *Langmuir* **11**, 4117 (1995).
12. F. GIRARD, M. ANTONI, and K. SEFIANE, *Langmuir* **24**, 9207 (2008).
13. H. HU and R. G. LARSON, *J. Phys. Chem. B* **110**, 7090 (2006).
14. K. SEFIANE, *Adv. Colloid Interface Sci.* **206**, 372 (2014).
15. C. V. STERNLING and L. E. SCRIVEN, *AIChE J.* **5**, 514 (1959).
16. A. D'AUBETERRE, R. DA SILVA, and M. E. AGUILERA, *Int. J. Heat Mass Transf.* **32**, 677 (2005).
17. P. LYFORD, H. PRATT, F. GREISER, and D. SHALLCROSS, *Can. J. Chem. Eng.* **76**, 167 (1998a).
18. P. LYFORD, H. PRATT, F. GREISER, and D. SHALLCROSS, *Can. J. Chem. Eng.* **76**, 175 (1998b).

-
19. R. S. SUBRAMANIAN and R. BALASUBRAMANIAN, *The motion of bubbles and drops in reduced gravity*, Cambridge University Press, 2001.
 20. N. O. YOUNG, J. S. GOLDSTEIN, and M. J. BLOCK, *J. Fluid Mech.* **6**, 350 (1959).
 21. S. C. HARDY, *J. Colloid Interface Sci.* **69**, 157 (1979).
 22. H. H. KIM and R. S. SUBRAMANIAN, *J. Colloid Interface Sci.* **127**, 417 (1989a).
 23. H. H. KIM and R. S. SUBRAMANIAN, *J. Colloid Interface Sci.* **130**, 112 (1989b).
 24. K. D. BARTON and R. S. SUBRAMANIAN, *J. Colloid Interface Sci.* **133**, 211 (1990).
 25. J. CHEN and K. J. STEBE, *J. Fluid Mech.* **340**, 35 (1997).
 26. J.-P. HANSEN and I. R. MCDONALD, *Theory of Simple Liquids*, Academic Press, 4 edition, 2013.
 27. F. VARNIK, J. BACHNAGEL, and K. BINDER, *J. Chem. Phys.* **113**, 4444 (2000).
 28. R. CLAUSIUS, *Phil. Mag.* **40**, 122 (1870), Engl. Trans.
 29. J. S. ROWLINSON and B. WIDOM, *Molecular Theory of Capillarity*, Clarendon Press, 1982.
 30. J. P. R. B. WALTON, D. J. TILDESLEY, J. S. ROWLINSON, and J. R. HENDERSON, *Mol. Phys.* **48**, 1357 (1983).
 31. J. G. KIRKWOOD and F. P. BUFF, *J. Chem. Phys.* **17**, 338 (1949).
 32. J. H. IRVING and J. G. KIRKWOOD, *J. Chem. Phys.* **18**, 817 (1950).
 33. S. PLIMPTON, *J. Comp. Phys* **117**, 1 (1995).
 34. E. DIAZ-HERRERA, G. RAMIREZ-SANTIAGO, and J. A. MORENO-RAZO, *J. Chem. Phys.* **123**, 184507 (2005).
 35. F. J. MARTÍNEZ-RUIZ, A. I. MORENO-VENTAS BRAVO, and F. J. BLAS, *J. Chem. Phys.* **143**, 104706 (2015).

-
36. D. FRENKEL and B. SMIT, *Understanding Molecular Simulation*, Academic Press, 2 edition, 1996.
 37. SCHNEIDER and STOLL, *Phys. Rev. B* **17**, 1302.
 38. H. C. ANDERSON, *J. Chem. Phys.* **72**, 2384 (1980).
 39. S. NOSÉ, *Mol. Phys.* **52**, 255 (1984).
 40. S. NOSÉ, *J. Chem. Phys.* **81**, 511 (1984).
 41. W. HOOVER, *Phys. Rev. A* **31**, 1695 (1985).
 42. B. SMIT, *J. Chem. Phys.* **96**, 8639 (1992).
 43. P. A. BOPP, J. B. BUHN, H. A. MAIER, and M. J. HAMPE, *Chem. Eng. Comm.* **195**, 1437 (2008).
 44. H. FLYVBJERG and H. PETERSEN, *J. Chem. Phys.* **91**, 461 (1989).
 45. A. J. HOWES and C. J. RADKE, *Langmuir* **23**, 1835 (2007).
 46. S. VAN DER WALT, S. C. COLBERT, and G. VAROQUAUX, *Comput. Sci. Eng.* **13**, 22 (2011).
 47. J. D. HUNTER, *Comput. Sci. Eng.* **9**, 90 (2007).
 48. A. MARCHAND, J. H. WEIJS, J. H. SNOEIJER, and B. ANDREOTTI, *Am. J. Phys.* **79**, 999 (2011).
 49. B. S. MASSEY, *Mechanics of Fluids*, CRC Press, 9 edition, 2012, Revised by J. Ward-Smith.